Spatial light modulation for interferometric scattering microscopy

Vivien Walter[1], Christopher Parperis[1], Yujie Guo[1], and Mark Ian Wallace[1,✉]

[1]Department of Chemistry, King's College London, Britannia House, 7 Trinity Street, London, UK

Interferometric scattering (iSCAT) microscopy enables high-speed and label-free detection of individual molecules and small nanoparticles. Here we apply point spread function engineering to provide adaptive control of iSCAT images using spatial light modulation. With this approach we demonstrate improved dynamic spatial filtering, real-time background subtraction, focus control, and signal modulation based on sample orientation.

Interferometric Scattering Microscopy | Spatial Light Modulation | PSF Engineering

Correspondence: ***mark.wallace@kcl.ac.uk***

Introduction

Interferometric scattering microscopy (iSCAT) is a sensitive label-free optical technique for imaging nanoscopic objects, including individual biomolecules (1–3). Notably it is a promising method with which to tackle some of the limitations of single-molecule fluorescence (SMF) microscopy. SMF methods have undoubtedly revolutionised our understanding of biology (4), and while advances in spatial and temporal resolution continue apace (5–7), the use of fluorescence as an image contrast mechanism presents some inherent experimental restrictions. For example, fluorescent labelling can alter biomolecule properties (8, 9), photobleaching prevents imaging for extended periods of time (10), and optical saturation provides a hard limit to the sampling rate at which a fluorescence process can be imaged (11). iSCAT circumvents the need for fluorescence labelling, relying instead on the interference between a local reference light field and the elastic scattering from an individual object (11). Although typically weaker, this signal is not subject to the same limitations and is dependent on wavelength, particle and medium permittivity, and volume.

Although in a shot-noise-limited measurement the SNR is independent of the contrast, small particle volumes understandably produce weak signals, and so image filtering is desirable to improve detection of small nanoparticles or single protein molecules. For example, control of the relative magnitude of scattered and reference signals has been reported as a mechanism to enhance the overall sensitivity of interferometric microscopy: Image contrast has been boosted by use of a half-silvered mirror to selectively reduce background signal in the output light path (12), and spatial filtering has been exploited, both by use of diaphragms (13) and partially-reflective metallic masks (14) to selectively attenuate spatial frequencies in the image, and hence control the overall detected contrast. A limitation to date is the fixed nature of the signal modulation these methods provide, with filtering engineered specifically for a given experiment. Spatial light modulators (SLMs) are a well established technology to provide dynamic, real-time control of the light field; widely applicable in microscopy (15). For example SLM-based adaptive optics can be used for aberration correction (16–19), and to achieve sub-diffraction-limited information; either by generating structured illumination fields (20, 21) or by re-engineering the point spread function (22). Similarly SLMs can be used as holographic lenses, to select focal planes and provide depth information (23–27).

Here we incorporate SLM control of the light field present in a reciprocal image plane for iSCAT microscopy. Specifically, we sought to quantify the potential of this method to provide adaptable, real-time control of contrast enhancement, focus, background subtraction and polarisation.

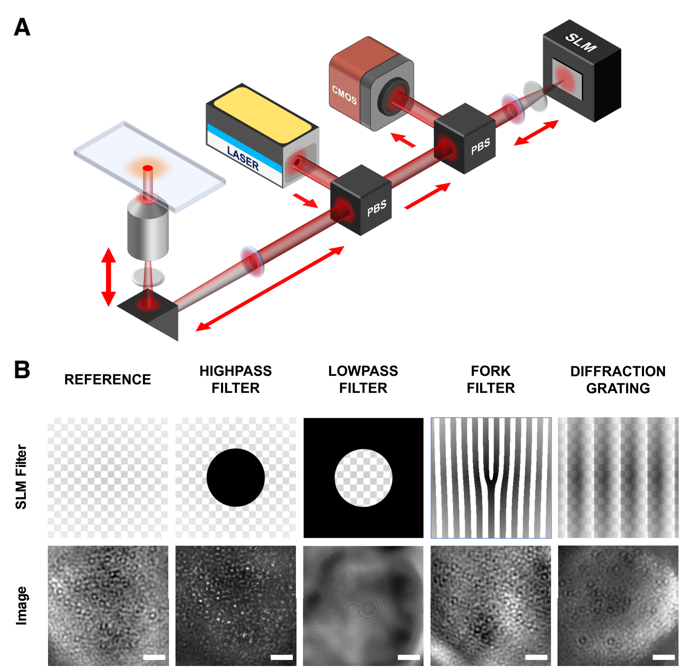

Fig. 1. (**A**) Simplified illustration of the iSCAT optical setup including the spatial light modulator (SLM) in the light path. Blue disks represent the main focussing/collimating lenses, while grey disks represent quarter wave plates. (**B**) A selection of different filter types that the SLM can project into frequency space. Top row: illustrations of filters as they are displayed on the SLM. Botton row: iSCAT response to each filter for samples of AuNPs (40 nm). Scale bars 4 µm.

Results

Instrument construction. A simplified illustration of the optical setup is shown in Fig.1A. Briefly: A a single-mode diode laser (640 nm, iBeam smart PT, Toptica, Munich GE), was directed into a microscope objective (Plan Apo $100\times/1.40$ Oil $\infty/0.17$ WD 0.13 DIC N2, Nikon) using a polarising beam splitter (PBS) and quarter-wave plate to isolate back scattering from the image and provide epi-illumination of the sample. A second PBS and quarter-wave plate was then used to project a conjugate back-focal plane onto a reflective SLM (920×1152 pixel, Meadowlark Optics, Frederick, CO, USA). Finally output from the SLM is returned through the second PBS and quarter wave plate to produce a focused image on a CMOS camera (MV1-D1024E-160-CL, Photonfocus, Lachen CH). XYZ position of the sample was controlled using a piezoelectric stage (P-545-3R8S, Physik Instrumente, Karlsruhe, GE). Other optomechanical components were purchased from Thorlabs (Newton, NJ, USA) or custom designed and fabricated.

The use of a SLM enables selective retardation of the optical wavefront at particular x,y positions, corresponding to each pixel of the device. When placed at a conjugate back focal plane, the SLM acts to induce a phase delay in undesired spatial frequencies, which are subsequently occluded by use of a quarter-wave plate and PBS. Patterns displayed on the SLM are filters which can be classified depending on the effect they have on the propagating wavefront. Fig.1B illustrates a range of potential applications for wavefront control. Filters include, but are not limited to, high-, low- and band-pass filters, which selectively suppress ranges of spatial frequencies above or below a predetermined threshold (28); fork filters, which may control the optical angular momentum of optical vortices (29); and diffraction gratings, which can induce a lateral shift to duplicate an image (30).

With our instrument established, we sought to quantify the effects of three specific filter types of interest in iSCAT microscopy: (1) background-reduction via high-pass filtering; (2) focus-control via Fresnel filters; and (3) orientation determination via directional filtering.

Contrast optimisation. Interference contrast can be optimised by controlling the relative magnitude of reference (background) intensity to that from a scattering object of interest (12). High-pass filtering is a simple spatial filter that removes a significant portion of the background intensity, along with typically unwanted low-frequency information while retaining the high-frequency signal of interest. By controlling the frequencies cut by the filter, the effective contrast can be controlled.

A sample of 5 nm gold particles was imaged on our iSCAT microscope. Different high-pass filters, consisting of black circles of varying diameter, were projected by the SLM and the subsequent images were recorded. Examples are shown in Fig.2A. The pixel diameters of each filter are reported as the corresponding occluded spatial frequencies.

Fig. 2 shows the measured dependence of in nanoparticle contrast with SLM high-pass filter frequency. These data were collected from ~100 nanoparticles over 3 samples. Nanoparticles were segmented using the TrackPy python module (31) with minimal intervention - simply analysing top 64% of pixel intensities following noise and background

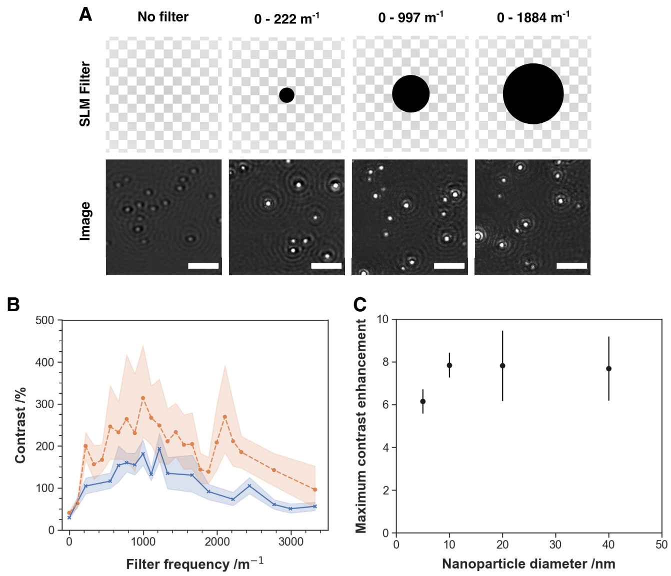

Fig. 2. (**A**) Effect of high-pass filtering on a sample of 5 nm AuNPs. Illustration of the corresponding filters are shown on the top row. Scale bars 3 µm. (**B**) Evolution of interference contrast with spatial frequency measured for two sizes of AuNP: 5 (blue) and 40 (red) nm. Markers represent the average contrast while the areas represent the respective 95% confidence interval. (**C**) Contrast enhancement factors for various AuNP sizes at the experimentally determined optimal high-pass frequency cutoff of 997 m^{-1}.

pre-processing. Here, contrast was determined by the division of the raw image by the background image following lateral displacement and median averaging (32). Removing spatial frequencies below 997 ± 55 m^{-1} provided the greatest increase in contrast (Fig.2B). The same optimal effective frequency cutoff was found for all AuNP samples (5, 10, 20, & 40 nm) using the same protocol (Fig.2C), providing a mean increase in contrast by a factor of 7 ± 4. The independence of optimal high-pass cutoff frequency and AuNP size is expected; as all particles are significantly below the diffraction limit, only the absolute contrast changes with nanoparticle size. Correspondingly, the factor by which each filter increases contrast is observed to be independent of object size. The variation of contrast with filter frequency is not a smooth function; we interpret the local variations in contrast with spatial frequency as due to the digital nature of the SLM spatial response across pixels.

To picture the effects of this spatial filter, consider the optimal cutoff frequency expressed as a spatial period - any feature of the image larger than 0.67 ± 0.04 µm will be filtered from the image. This optimal spatial extent is, unsurprisingly, similar to the width of the point spread function of our imaging system ($\sigma \approx 0.61 \pm 0.04$ µm, Fig.S1).

Focus control. Encoding Fresnel patterns on the SLM converts the device into a diffraction-based lens, enabling the SLM to rapidly select the focal plane which forms an image on the CMOS detector. Thus for a fixed distance between the objective and the sample, modification of Fresnel pattern properties in turn modifies the position of the object plane, emulating axial movement of the objective lens relative to the sample. A representative example of use of the SLM for focus adjustment is presented in Fig.3A. 40 nm AuNPs bound

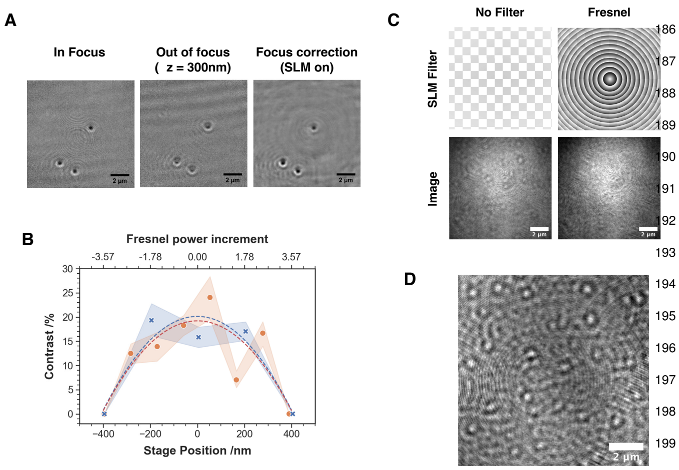

Fig. 3. (**A**) Sample of 40 nm AuNPs, first brought into focus (left) and then drifted out of focus by 300 nm (center) using the microscope stage. The particles are brought back into focus (right) using a Fresnel pattern and no movement of the stage. (**B**) Evolution of image contrast for 40 nm gold particles using different Fresnel patterns at fixed stage position (red) or different stage positions with no Fresnel pattern applied (blue). Markers represent the average contrast while the areas represent the respective CI 95 of the markers determined for 40 nanoparticles. (**C**) Unprocessed images of a AuNP sample entirely defocused upon projection of a the Fresnel pattern. (**D**) Result of subtracting the defocused image from the in-focus image. We propose this strategy as a method for real-time background correction, equally effective for imaging either diffusing or static objects.

to a microscope coverslip were brought into focus using the piezoelectric stage. Subsequently, a 300 nm translation of the piezoelectric stage defocused the sample. A Fresnel zone plate was then created on the SLM to restore focus.

A Fresnel pattern is defined by its radius, R_f, and power, p_f (see equation (1) and (2) Supplementary Information) with focus control determined by changes in these parameters (33). While R_f is an integer due to the discrete pixellated nature of the SLM, p_f is a real number than can take any value. To quantify the focus control in our system, the evolution of image contrast for 40 nm AuNP was plotted as a function of p_f. We compared these data with the evolution of image contrast as a function of z axis movement caused by a direct translation of the sample using the piezoelectric stage (Fig.3B). Specific SLM patterns are depicted in Fig.S2&3 of the Supplementary Information. As our SLM is an 8-bit digital device, ultimately we are limited to step changes in p_f of 1/256, hence $\delta p_f \approx 0.004$ (see equation (1) and (2) of the Supplementary Information). With reference to the calibration curve in Fig.3A, this corresponds to a theoretical change in the focal plane position δz = 0.45 nm. For comparison, our piezoelectric control of z has a precision of δz = 100 nm. Focus control using the SLM has another benefit besides this improved precision; no mechanical part is required to move. Fast focus control is possible - limited by the refresh rate of the SLM display (30 Hz in our current setup, but other commercially available SLMs can achieve rates above 500 Hz), rather than relying on piezo-control of focussing (here, $\approx$ 2.5Hz).

Background correction. In addition to direct focus control, we also considered the use of Fresnel patterns for fast on-the-fly background correction for iSCAT. Detection in iSCAT is often challenging due to the small fractional contrast associated with the interferometric scattering, and thus can be lost in background noise (typically $\leq 1\%$). To some extent this problem is alleviated by post-processing, typically by median image division. However this is difficult to implement during image acquisition as: (i) it requires many images to be averaged (> 100), (ii) computing the median image for subsequent stack division is time consuming and negatively impacts frame rate, (iii) background correction by median division removes static objects that may be of interest from the image. Post-processing Gaussian blurring has previously been used to provide a simple, means of background correction (34). Here we exploit the fast defocusing provided by Fresnel zone plates to provide background correction which is unencumbered by these typical drawbacks. Background correction by SLM fast defocusing does however represent a trade-off and slower methods of excluding background by sample spatial or temporal displacement typically provide more efficient correction.

We again, examined 40 nm AuNPs using the same particle detection conditions and preparation methods as used in 2. A focused iSCAT image was collected and then a Fresnel pattern was applied to completely defocus the image, such that objects are no longer discernible while the pattern is displayed. Background correction is then simply achieved by processing in which the Fresnel pattern is consecutively applied and removed at a frequency equal to the frame rate of image acquisition of the camera detector. Alternating images, in and out of focus, are recorded by the camera, and the live focused image is continuously divided by the defocused image. An example of the corrected image this process would produce is given in Figure 3(C)). Since only two frames are required for this live background correction, we achieve a final frame rate of 30 Hz. Faster rates than this would be easily accessible with other pairings of CMOS detectors and SLM displays.

Orientation detection. In addition to directionless bandpass filters, the SLM can be used to manipulate the Fourier space in an optical setup to select only a specific direction of the spatial frequency and cut all the other directions. Effectively, this results in an interference contrast reduction in the image in real space for all objects which have an orientation different to the one selected in the filter.

Gold nanorods (AuNR) (length 40 nm, diameter 25 nm), chosen for their strong directional scattering due to their symmetry, were spin-coated on a glass coverslip and imaged with the iSCAT. Because of their diffraction-limited size, the AuNR appear similar to spherical nanoparticles (Fig.4A) and it is not possible to tell their orientation directly from the image. A directional filter, consisting of a band of predetermined angle and thickness centred on the SLM display, was projected at varying angles. The image response to SLM band rotation is show in Fig.4B. The contrast of individual objects changed when the filter was rotated, eventually leading to individual particles completely disappearing from the image for certain orientations of the filter. Modulation of particle contrast upon filter rotation was not observed for spherical particles (Fig.

S4).

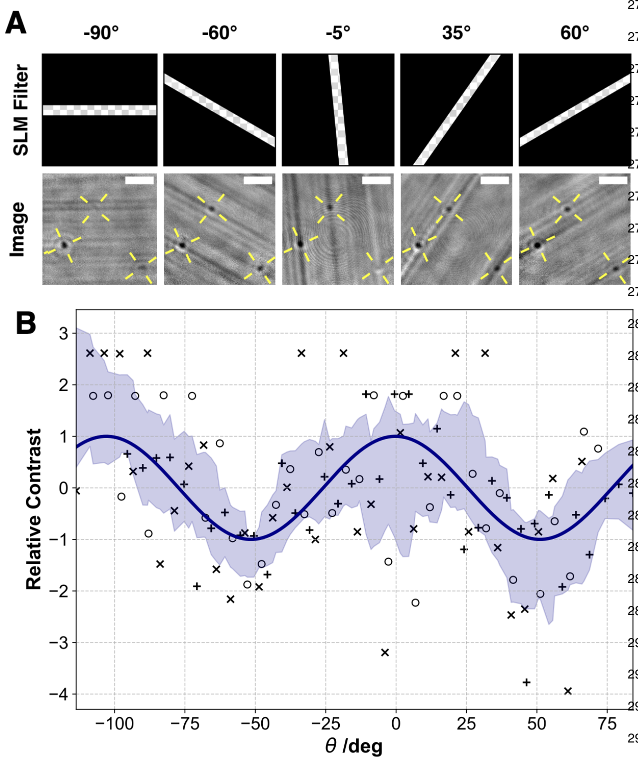

Fig. 4. (**A**) Effect of linear filters set at different angles on visualizing a sample of AuNR. Illustration of the corresponding filters are shown on the top row. The yellow axes show the measured orientation of the corresponding objects. Scale bar is 2 µm. (**B**) Evolution of the contrast of gold AuNR with the filter angle θ projected on the SLM. Each marker is a single data point, markers correspond to different AuNRs, area is the standard deviation CI, and the blue line is the sine fit of the individual points.

Measurement of contrast evolution for the AuNR was executed by rotating the SLM-projected band at intervals of 5° between -90° and +90°. A total rotation of 180° was selected because we assumed the AuNR would behave with rotational symmetry of order 2 so all possible rotations can be described between 0° and 180°. These data show diffraction limit particles, whose individual contast varies with the rotation of the SLM filter. Different AuNR reaching maxima at different rotations, corresponding to their (random) orientation on the surface. The angular dependence of contrast for individual AuNR, randomly orientated particles were combined by aligning signal maxima - effectively 'phase-shifted' all signals to match one another, then merged for an ensemble evolution of the signal and its period. Results are shown in Figure 4. The angular dependence of the relative contrast of the particles evolve in a sine wave shape with the orientation of the filter. A fit of the raw data of relative contrast using a simple sine function returns a period close to 90°. AuNR have 2 main axes of line symmetry, perpendicular to each other, which would be expected to correspond to 90 degree rotations of the directional filter. Our observations are consistent with signals modulating between these two contrast maxima every $\sim 90°$, with an intermediate minima at $\sim 45°$ to both axes.

Conclusions

In these experiments we have sought to evaluate the usefullness of PSF engineering for iSCAT microscopy. The direct dynamic access to the frequency domain of an image provided by SLMs offer many possibilities for interference contrast enhancement, background removal, and access to additional information, such as sub-diffraction limited particle orientation. The use of iSCAT SLM provides speed, precision, and versatile filtering without macroscopic perturbation of the optical system. Here, our use of high-pass filtering showed a size-independent optimal frequency as we chose to maintain sample consistency across the use of different filters. For non-diffraction limited objects, however, we expect dynamic control of spatial frequency cutoff would become increasingly important. We used linear filters to determine the orientation of diffraction limited AuNR, however the temporal modulation in intensity provided by this approach might also provide a future route to optical heterodyne detection of iSCAT signals.

Beyond the applications covered in this work, we foresee numerous possibilities for implementations relevant to interferometric microscopy, exploiting the large diversity of PSF engineering available: For instance, a displayed diffraction grating pattern can produce image duplicates to process features in parallel (35); A VanderLugt correlator might be applied to detect specific features in the sample (36); Label-free 3D particle tracking is also becoming an area of interest in iSCAT research (37), and we see the SLM as having potential for adaptive wavefront control to enable future 3D applications.

Methods

Materials. Gold nanoparticles (AuNPs) of size ranging from 5 to 40 nm, gold nanorods (AuNRs) of length 40 nm, diameter 25 nm, and solvents used in this work were purchased from Sigma-Aldrich (now Merck, Darmstadt, GE).

Sample preparation. Borosilicate glass coverslips (24×60 mm, #1 thickness, Menzel Gläser) were sonicated for 15 minutes in Decon 90 (10% v/v, Fisher Scientific, Hampton, NH, USA) and washed 8× in purified water (Millipore Direct-Q UV3, Merck). Coverslips were sonicated for a further 15 minutes in water, washed 8× in water, and stored in isopropyl alcohol.

Coverslips were dried under a stream of nitrogen and treated with an oxygen plasma for 5 minutes (Diener Electronic, 90 W, 0.5 bar oxygen flow). Following cleaning, AuNPs were sonicated for 2 minutes to encourage breakup of particle aggregates. Coverslips were then spin coated at 4000 rpm for 30 s (Laurell WS-650MZ-23NPPB) with 2× 50 µL volumes of AuNP suspension without further dilution.

To image the sample, a silicon spacer (Coverwell, Grace Bio-Lab, Bend, OR USA) was installed on top of the coverslip and filled with water. A second coverslip (18 mm diameter, Chongqing New World Trading Co.) was cleaned using the procedure described above. The top of the observation chamber was then sealed with this coverslip.

Image acquisition and analysis. Data acquisition was controlled using LabVIEW (National Instruments, Austin TX USA). For the data presented here, 300 frames were recorded at 150 Hz. Laser power was set to the maximum available (80 mW). The exposure time of the camera was then set automatically by our control software to ensure the maximum pixel value detected was 85 to 90% of the pixel full well capacity of the detector to prevent saturation and maximise the accuracy of the contrast measurement.

Image analysis was performed using Python scripts developed in-house. All measurement were preceded by image normalisation via division of each frame by the median-averaged projection. Particles were then located using the Python module TrackPy (31). Where required, a linear profile was plotted across the particle and fitted using a sinc function. The amplitude of the fitted sinc determines the measured intensity of particle signal (I_s) and background (I_b) respectively. Particle contrast was calculated as $C = (I_s - I_b)/I_b$.

ACKNOWLEDGEMENTS

The authors acknowledge support from the BBSRC (BB/R001790/1). MIW is supported by a Wellcome Trust Investigator Award in Science (224327/Z/21/Z). CP is supported with funding from Oxford Nanopore Technologies. The authors thank Dr Pantelitsa Dimitriou for their help in preparing the revision of this manuscript.

Bibliography

1. K Lindfors, T Kalkbrenner, P Stoller, and V Sandoghdar. Detection and Spectroscopy of Gold Nanoparticles Using Supercontinuum White Light Confocal Microscopy. *Physical Review Letters*, 93(3):37401, jul 2004. doi: 10.1103/PhysRevLett.93.037401.
2. Marek Piliarik and Vahid Sandoghdar. Direct optical sensing of single unlabelled proteins and super-resolution imaging of their binding sites. *Nature Communications*, 5(1):4495, 2014. doi: 10.1038/ncomms5495.
3. Gavin Young, Nikolas Hundt, Daniel Cole, Adam Fineberg, Joanna Andrecka, Andrew Tyler, Anna Olerinyova, Ayla Ansari, Erik G Marklund, Miranda P Collier, Shane A Chandler, Olga Tkachenko, Joel Allen, Max Crispin, Neil Billington, Yasuharu Takagi, James R Sellers, Cédric Eichmann, Philipp Selenko, Lukas Frey, Roland Riek, Martin R Galpin, Weston B Struwe, Justin L P Benesch, and Philipp Kukura. Quantitative mass imaging of single biological macromolecules. *Science*, 360(6387):423–427, apr 2018. doi: 10.1126/science.aar5839.
4. Sviatlana Shashkova and Mark C Leake. Single-molecule fluorescence microscopy review: shedding new light on old problems. *Bioscience reports*, 37(4), jul 2017. doi: 10.1042/BSR20170031.
5. Eric Betzig, George H Patterson, Rachid Sougrat, O Wolf Lindwasser, Scott Olenych, Juan S Bonifacino, Michael W Davidson, Jennifer Lippincott-Schwartz, and Harald F Hess. Imaging Intracellular Fluorescent Proteins at Nanometer Resolution. *Science*, 313(5793): 1642 LP – 1645, sep 2006. doi: 10.1126/science.1127344.
6. Klaus C. Gwosch, Jasmin K. Pape, Francisco Balzarotti, Philipp Hoess, Jan Ellenberg, Jonas Ries, and Stefan W. Hell. MINFLUX nanoscopy delivers 3D multicolor nanometer resolution in cells. *Nature Methods*, 17(2):217–224, 2020. doi: 10.1038/s41592-019-0688-0.
7. Luciano A Masullo, Florian Steiner, Jonas Zähringer, Lucía F Lopez, Johann Bohlen, Lars Richter, Fiona Cole, Philip Tinnefeld, and Fernando D Stefani. Pulsed Interleaved MINFLUX. *Nano Letters*, 21(1):840–846, jan 2021. doi: 10.1021/acs.nanolett.0c04600.
8. Manuel P Luitz, Anders Barth, Alvaro H Crevenna, Rainer Bomblies, Don C Lamb, and Martin Zacharias. Covalent dye attachment influences the dynamics and conformational properties of flexible peptides. *PloS one*, 12(5):e0177139–e0177139, may 2017. doi: 10.1371/journal.pone.0177139.
9. Muhammad Jan Akhunzada, Francesca D'Autilia, Balasubramanian Chandramouli, Nicholus Bhattacharjee, Andrea Catte, Roberto Di Rienzo, Francesco Cardarelli, and Giuseppe Brancato. Interplay between lipid lateral diffusion, dye concentration and membrane permeability unveiled by a combined spectroscopic and computational study of a model lipid bilayer. *Scientific Reports*, 9(1):1508, 2019. doi: 10.1038/s41598-018-37814-x.
10. Hui Zhang and Peixuan Guo. Single molecule photobleaching (SMPB) technology for counting of RNA, DNA, protein and other molecules in nanoparticles and biological complexes by TIRF instrumentation. *Methods (San Diego, Calif.)*, 67(2):169–176, may 2014. doi: 10.1016/j.ymeth.2014.01.010.
11. Richard W Taylor and Vahid Sandoghdar. Interferometric Scattering Microscopy: Seeing Single Nanoparticles and Molecules via Rayleigh Scattering. *Nano Letters*, 19(8):4827–4835, aug 2019. doi: 10.1021/acs.nanolett.9b01822.
12. Daniel Cole, Gavin Young, Alexander Weigel, Aleksandar Sebesta, and Philipp Kukura. Label-Free Single-Molecule Imaging with Numerical-Aperture-Shaped Interferometric Scattering Microscopy. *ACS Photonics*, 4(2):211–216, feb 2017. doi: 10.1021/acsphotonics.6b00912.
13. Oguzhan Avci, Maria I Campana, Celalettin Yurdakul, and M Selim Ünlü. Pupil function engineering for enhanced nanoparticle visibility in wide-field interferometric microscopy. *Optica*, 4(2):247–254, 2017. doi: 10.1364/OPTICA.4.000247.
14. Matz Liebel, James T Hugall, and Niek F van Hulst. Ultrasensitive Label-Free Nanosensing and High-Speed Tracking of Single Proteins. *Nano Letters*, 17(2):1277–1281, feb 2017. doi: 10.1021/acs.nanolett.6b05040.
15. C Maurer, A Jesacher, S Bernet, and M Ritsch-Marte. What spatial light modulators can do for optical microscopy. *Laser & Photonics Reviews*, 5(1):81–101, jan 2011. doi: https://doi.org/10.1002/lpor.200900047.
16. Tsung-Li Liu, Srigokul Upadhyayula, Daniel E Milkie, Ved Singh, Kai Wang, Ian A Swinburne, Kishore R Mosaliganti, Zach M Collins, Tom W Hiscock, Jamien Shea, Abraham Q Kohrman, Taylor N Medwig, Daphne Dambournet, Ryan Forster, Brian Cunniff, Yuan Ruan, Hanako Yashiro, Steffen Scholpp, Elliot M Meyerowitz, Dirk Hockemeyer, David G Drubin, Benjamin L Martin, David Q Matus, Minoru Koyama, Sean G Megason, Tom Kirchhausen, and Eric Betzig. Observing the cell in its native state: Imaging subcellular dynamics in multicellular organisms. *Science*, 360(6386), apr 2018. doi: 10.1126/science.aaq1392.
17. Naoya Matsumoto, Alu Konno, Takashi Inoue, and Shigetoshi Okazaki. Aberration correction considering curved sample surface shape for non-contact two-photon excitation microscopy with spatial light modulator. *Scientific Reports*, 8(1):9252, 2018. doi: 10.1038/s41598-018-27693-7.
18. Naoya Matsumoto, Alu Konno, Yasushi Ohbayashi, Takashi Inoue, Akiyuki Matsumoto, Kenji Uchimura, Kenji Kadomatsu, and Shigetoshi Okazaki. Correction of spherical aberration in multi-focal multiphoton microscopy with spatial light modulator. *Optics Express*, 25(6): 7055–7068, 2017. doi: 10.1364/OE.25.007055.
19. M A A Neil, R Juškaitis, M J Booth, T Wilson, T Tanaka, and S Kawata. Adaptive aberration correction in a two-photon microscope. *Journal of Microscopy*, 200(2):105–108, nov 2000. doi: https://doi.org/10.1046/j.1365-2818.2000.00770.x.
20. Jeong-Heon Han, Nak-Won Yoo, Ji-Hoon Kang, Byeong-Kwon Ju, and Min-Chul Park. Optimization of structured illumination microscopy with designing and rotating a grid pattern using a spatial light modulator. *Optical Engineering*, 58(9):1–8, sep 2019. doi: 10.1117/1.OE.58.9.094102.
21. Ronny Förster, Hui-Wen Lu-Walther, Aurélie Jost, Martin Kielhorn, Kai Wicker, and Rainer Heintzmann. Simple structured illumination microscope setup with high acquisition speed by using a spatial light modulator. *Optics Express*, 22(17):20663–20677, 2014. doi: 10.1364/OE.22.020663.
22. Sri Rama Prasanna Pavani, Michael A Thompson, Julie S Biteen, Samuel J Lord, Na Liu, Robert J Twieg, Rafael Piestun, and W E Moerner. Three-dimensional, single-molecule fluorescence imaging beyond the diffraction limit by using a double-helix point spread function. *Proceedings of the National Academy of Sciences*, 106(9):2995 LP – 2999, mar 2009. doi: 10.1073/pnas.0900245106.
23. Luis Camacho, Vicente Micó, Zeev Zalevsky, and Javier García. Quantitative phase microscopy using defocusing by means of a spatial light modulator. *Optics Express*, 18(7): 6755–6766, 2010. doi: 10.1364/OE.18.006755.
24. Hui Zhu, Kapil Dev, and Anand Asundi. Design and characterization of DOE micro lens array for spatial light modulator. *Physics Procedia*, 19:139–145, 2011. doi: https://doi.org/10.1016/j.phpro.2011.06.138.
25. Kunlachat Ayutthaya, Pradit Mittrapiyanuruk, and Pakorn Kaewtrakulpong. Adaptive Focal Length Imaging System using Liquid Crystal Spatial Light Modulator. *Indian Journal of Science and Technology*, 9, dec 2016. doi: 10.17485/ijst/2016/v9i48/109312.
26. M P Lee, G M Gibson, R Bowman, S Bernet, M Ritsch-Marte, D B Phillips, and M J Padgett. A multi-modal stereo microscope based on a spatial light modulator. *Optics Express*, 21 (14):16541–16551, 2013. doi: 10.1364/OE.21.016541.
27. Rui Liu, Neil Ball, James Brockill, Leonard Kuan, Daniel Millman, Cassandra White, Arielle Leon, Derric Williams, Shig Nishiwaki, Saskia de Vries, Josh Larkin, David Sullivan, Cliff Slaughterbeck, Colin Farrell, and Peter Saggau. Aberration-free multi-plane imaging of neural activity from the mammalian brain using a fast-switching liquid crystal spatial light modulator. *Biomedical Optics Express*, 10(10):5059–5080, 2019. doi: 10.1364/BOE.10.005059.
28. J Jeong, I W Jung, H J Jung, D M Baney, and O Solgaard. Multifunctional Tunable Optical Filter Using MEMS Spatial Light Modulator. *Journal of Microelectromechanical Systems*, 19(3):610–618, 2010. doi: 10.1109/JMEMS.2010.2043641.
29. Jun Liu and Jian Wang. Demonstration of polarization-insensitive spatial light modulation using a single polarization-sensitive spatial light modulator. *Scientific Reports*, 5(1):9959, 2015. doi: 10.1038/srep09959.
30. R Bowman, V D'Ambrosio, E Rubino, O Jedrkiewicz, P Di Trapani, and M J Padgett. Optimisation of a low cost SLM for diffraction efficiency and ghost order suppression. *The European Physical Journal Special Topics*, 199(1):149–158, 2011. doi: 10.1140/epjst/e2011-01510-4.
31. TrackPy Zenodo repo, 2019.
32. Jaime Ortega Arroyo, Daniel Cole, and Philipp Kukura. Interferometric scattering microscopy and its combination with single-molecule fluorescence imaging. *Nature protocols*, 11(4):617–633, 2016.
33. Lenny A Romero, María S Millán, and Elisabet Pérez-Cabré. Optical implementation of multifocal programmable lens with single and multiple axes. *Journal of Physics: Conference Series*, 274:12050, 2011. doi: 10.1088/1742-6596/274/1/012050.
34. Georgios Babaloukas, Nicholas Tentolouris, Stavros Liatis, Alexandra Sklavounou, and Despoina Perrea. Evaluation of three methods for retrospective correction of vignetting on medical microscopy images utilizing two open source software tools. *Journal of Microscopy*, 244(3):320–324, dec 2011. doi: https://doi.org/10.1111/j.1365-2818.2011.03546.x.
35. Jeffrey A Davis, Ignacio Moreno, María M Sánchez-López, Katherine Badham, Jorge Albero, and Don M Cottrell. Diffraction gratings generating orders with selective states of polarization. *Optics Express*, 24(2):907–917, 2016. doi: 10.1364/OE.24.000907.
36. Xu Zeng, Jian Bai, Changlun Hou, and Guoguang Yang. Compact optical correlator based on one phase-only spatial light modulator. *Optics Letters*, 36(8):1383–1385, 2011. doi: 10.1364/OL.36.001383.
37. Richard W Taylor, Cornelia Holler, Reza Gholami Mahmoodabadi, Michelle Küppers, Houman Mirzaalian Dastjerdi, Vasily Zaburdaev, Alexandra Schambony, and Vahid San-

doghdar. High-Precision Protein-Tracking With Interferometric Scattering Microscopy , 2020.